

# A Bayesian regularization-backpropagation neural network model for peeling computations

Saipraneeth Gouravaraju<sup>a</sup>, Jyotindra Narayan<sup>a</sup>, Roger A. Sauer<sup>b,c,d</sup> and Sachin Singh Gautam<sup>a,\*</sup>

<sup>a</sup>Department of Mechanical Engineering, Indian Institute of Technology Guwahati, Guwahati, Assam 781039, INDIA

<sup>b</sup>Graduate School, Aachen Institute for Advanced Study in Computational Engineering Science (AICES), RWTH Aachen University, Templergraben 55, 52056 Aachen, GERMANY

<sup>c</sup>Department of Mechanical Engineering, Indian Institute of Technology Kanpur, UP 208016, INDIA

<sup>d</sup> Faculty of Civil and Environmental Engineering, Gdańsk University of Technology, ul. Narutowicza 11/12, 80-233 Gdańsk, Poland

## ARTICLE INFO

Keywords:

Machine learning

Adhesion

Peeling

Artificial neural networks

Bayesian regularization

## ABSTRACT

Bayesian regularization-backpropagation neural network (BR-BPNN) model is employed to predict some aspects of the gecko spatula peeling viz. the variation of the maximum normal and tangential pull-off forces and the resultant force angle at detachment with the peeling angle. K-fold cross validation is used to improve the effectiveness of the model. The input data is taken from finite element (FE) peeling results. The neural network is trained with 75% of the FE dataset. The remaining 25% are utilized to predict the peeling behavior. The training performance is evaluated for every change in the number of hidden layer neurons to determine the optimal network structure. The relative error is calculated to draw a clear comparison between predicted and FE results. It is shown that the BR-BPNN model in conjunction with k-fold technique has significant potential to estimate the peeling behavior.

## 1. Introduction

The study of peeling is essential in understanding the adhesion characteristics in many applications such as adhesive tapes, micro- and nano-electronics [1, 2], coatings [3], microfiber arrays [4, 5], wearable medical bands [6], and cell adhesion [7]. Peeling problems have been used by many researchers to analyze multiscale adhesion in biological adhesive pads such as in geckos, insects, and spiders [8–11], where peeling is an important aspect of detachment. For example, the nanoscale spatulae in geckos are very thin structures (approximately 5 – 10 nm thick) with a width of around 200 nm that can be modeled effectively as a thin strip [12–15]. These nanoscale structures interact with substrates through short-range van der Waals forces [16]. Peeling of the various components in the hierarchical microstructure of the adhesive pads have been studied extensively using analytical [12, 17, 18], experimental [16, 19–21], and numerical models [14, 15, 22, 23] to gain new insight into their mechanics. Several researchers used thin film peeling models to understand various aspects of gecko adhesion such as reversible adhesion [22, 24], pre-straining [18, 25, 26], dynamic self-cleaning [27], and adhesive friction [10, 28–30]. Adhesion and peeling of multiscale biological adhesives is a particularly complex phenomenon that is influenced by a wide variety of geometrical, material, and environmental parameters [15, 31–33]. Computational methods provide an opportunity to utilize a single framework to study the effect of these various factors [34].

Machine learning techniques have found applications in a wide range of data driven research areas including computational mechanics [35–41]. The probabilistic and flexible nature of machine learning enhances the capabilities of conventional computational models. Artificial neural network (ANN) is one of such successful statistical methods that has been used in various engineering problems to analyze discrete data and find complex interrelations therein [42–45]. ANNs are modeled to mimic the neural network in a brain, such that each artificial neuron communicates with other connected artificial neurons similar to synapses in the brain [46]. ANNs have been employed to study various problems in the computational mechanics, such as inverse problems [47, 48], constitutive modelling [49–51], fracture [52], and damage detection [53, 54]. Using ANNs, Manevitz et al. [55] predicted the optimal placement of

\*Corresponding author

✉ saipraneeth@iitg.ac.in (S. Gouravaraju); n.jyotindra@gmail.com (J. Narayan); sauer@aices.rwth-aachen.de (R.A. Sauer); ssg@iitg.ac.in (S.S. Gautam)

🌐 [www.iitg.ac.in/ssg](http://www.iitg.ac.in/ssg) (S.S. Gautam)

ORCID(s): 0000-0001-5625-8295 (R.A. Sauer); 0000-0001-7853-0253 (S.S. Gautam)

nodes on a two-dimensional geometry to generate a finite element mesh. Rapetto et al. [56] employed ANNs to predict the relationship between the surface roughness parameters and the real contact area in elastic contact between a rough surface and a flat rigid substrate. Gyurova et al. [57] predicted sliding friction and wear characteristics of polymer composites using ANNs. Liang et al. [45] proposed a fast and accurate method based on deep learning to estimate the stress distribution in aortic walls of the human heart. Hamdia et al. [58] used a deep neural network algorithm to understand the material response of a flexoelectric cantilever nanobeam. They obtained the data for training by solving the governing differential equations using NURBS based isogeometric analysis. Gu et al. [59] used neural networks to propose a new design methodology for bio-inspired hierarchical composite materials. The designs are optimized based on strength and toughness of the materials. Finite element (FE) analysis is used to obtain the training and testing data. They have shown that employing neural networks can significantly reduce the high computational cost of FE simulations. It was observed that their neural network could evaluate billions of material designs in a matter of hours, for which the finite element method would take years to solve. Oishi and Yoshimura [60] proposed a new local node-to-segment contact search method using deep neural networks to reduce the high computation time involved. Recently, this work has been extended by Oishi and Yagawa [61] to surface-to-surface local contact search between arbitrarily curved surfaces, which are described by non-uniform rational B-spline (NURBS) basis functions. Nowell and Nowell [62] used ANNs to predict the total fretting fatigue life of an aluminium alloy. Using deep learning techniques, Kim et al. [63] performed shape optimization to design adhesive pillars with uniform stress distribution and high adhesive strength. The deep neural networks combined with genetic optimization could predict the stress distribution in the interface and the detachment mechanism with great accuracy and computational efficiency. Khoei et al. [64] used backpropagation learning method based neural network with Nelder-Mead method [65], to develop a novel efficient stress recovery technique in adaptive finite element method. It was observed that their neural network model performed much better than the conventional superconvergent patch recovery (SPR) technique and weighted superconvergent patch recovery (WSPR) technique, especially in regions of high stress-concentrations.

Backpropagation algorithms are extensively used to train neural networks [66] in machine learning. In case of ANNs, to minimize the error associated with backpropagation algorithms, several generalization methods such as Bayesian regularization (BR) [67, 68] and Levenberg–Marquardt (LM) [69] are used. Generalization methods also minimize the likelihood of overfitting the training data. Both the BR and LM methods are often employed owing to their advantage in obtaining a lower mean squared error [70]. However, it has been observed that Bayesian regularization performs better than LM [70] with BR achieving highest correlation coefficient and lowest sum of square errors. As such, Bayesian regularization has been employed to successfully study various problems such as constitutive modeling, data mining, predicting stock price movement, magnetic shielding, and chemical adsorption [71–75]. To the best of the authors' knowledge there has been no study which employs machine learning techniques to analyze adhesive peeling and specifically gecko spatula peeling.

Peeling problems, particularly gecko spatula peeling, have been studied extensively using experimental, analytical, and computational methods. However, each of these methods come with their specific limitations. Although experimental investigations provide insights into the gecko adhesive system, they have been limited only down to the seta level. To the authors' best knowledge, there have been no experimental studies that explored the adhesive and frictional behaviour at the spatula level owing to the difficulty in isolating a single spatula. Most of the analytical models that study the peeling of gecko spatulae, though they provide insights into the various aspects of the peeling behaviour, they are also limited by their inherent assumptions such as steady-state peeling, nonzero bending stiffness, and linear material response. As such, most of the analytical models are unable to predict the entire peel-off process, including the snap-off behaviour. This necessitates the use of a numerical analysis tool like FEM. However, the computational cost can become very high due to the nonlinear and small scale nature of molecular adhesion as well as the detailed spatula microstructure. The high computational cost can be overcome by reduced models, such as beam models [76], but the cost remains a major limitation of full continuum models. As observed by some authors [59, 61, 63], the use of machine learning techniques such as artificial neural networks has the potential to reduce these computational costs while retaining the accuracy of numerical methods. Recently, Gouravaraju et al. [30, 77] have studied the peeling behaviour of a single gecko spatula. However, as mentioned above, the computational cost of the numerical model is very high. Therefore, in this paper, Bayesian regularization based backpropagation neural networks are employed to predict the influence of the peeling angle on the peeling force of a gecko spatula. The input data is obtained from the finite element simulations of Gouravaraju et al. [30, 77], who have used a quasi-continuum finite element model that captures friction due to adhesion at the nanoscale [78, 79].

The remainder of the paper is structured as follows: Section 2 discusses the adhesive friction model and the peeling

of the spatula. In section 3 a backpropagation neural network with Bayesian regularization is presented. Section 4 discusses the implementation of the neural network model. Results and discussion are presented in section 5. Finally, section 6 concludes the paper.

## 2. Peeling using an adhesive friction model

In this section, the adhesive friction model of Mergel et al. [79] and its application to gecko spatula peeling by Gouravaraju et al. [30, 77] are briefly described.

The "Model EA" of Mergel et al. [79] defines a sliding traction threshold  $T_s$  that is non-zero even for tensile normal forces. This sliding threshold depends on the magnitude of the normal traction  $T_n = \|\mathbf{T}_n\|$  due to adhesion between the spatula and the substrate. Further, it is assumed that the interfacial frictional forces act only up to a certain cut-off distance  $r_c$ . Then we have,

$$T_s(r) = \begin{cases} \frac{\mu_f}{J_c} [T_n(r) - T_n(r_c)], & r < r_c, \\ 0, & r \geq r_c, \end{cases} \quad (1)$$

where  $J_c$  is the local contact surface stretch ( $= 1$  for rigid substrates),  $\mu_f$  is the friction coefficient, and  $r$  denotes the minimum distance between the interacting surfaces.

The normal traction  $T_n$  is obtained from the variation of the total adhesion potential, which is the summation of individual adhesion potentials acting between the molecules of the substrate and the spatula, and is given as [80]

$$\mathbf{T}_n = \frac{A}{2\pi r_0^3} \left[ \frac{1}{45} \left( \frac{r_0}{r} \right)^9 - \frac{1}{3} \left( \frac{r_0}{r} \right)^3 \right] \mathbf{n}_s, \quad (2)$$

where  $r_0$  is the equilibrium distance of the Lennard-Jones potential,  $A$  is Hamaker's constant, and  $\mathbf{n}_s$  is the normal to the substrate.

Similar to Coulomb's friction model, the magnitude of frictional traction  $\mathbf{T}_f$  is governed by

$$\|\mathbf{T}_f\| \begin{cases} < T_s & \text{for sticking,} \\ = T_s & \text{for sliding,} \end{cases} \quad (3)$$

and is computed using a predictor-corrector algorithm [30]. A Neo-Hookean material model is employed to model the spatula response [81]. For further details on the application of the adhesive friction model, we refer to Gouravaraju et al. [30].

The spatula is modeled as a thin two-dimensional strip as shown in Fig. 1. A displacement  $\bar{\mathbf{u}}$  is applied to the spatula shaft at an angle called the peeling angle  $\theta_p$ . Nonlinear finite element analysis is employed to solve the resulting mechanical boundary value problem given by the nonlinear equation

$$\mathbf{f}(\mathbf{u}) := \mathbf{f}_{\text{int}} + \mathbf{f}_c = \mathbf{0}, \quad (4)$$

where  $\mathbf{f}_{\text{int}}$  and  $\mathbf{f}_c$  are the global internal and contact force vectors. The spatula is divided into  $240 \times 12$  finite elements along  $x$  and  $y$  directions, respectively. To accurately capture the nonlinear contact tractions (see Eqs. (1) and (2)), a local enrichment strategy proposed by Sauer [82] is employed. In this strategy, the contact surface is discretized using fourth-order Lagrange polynomials while the bulk is discretized using the standard linear Lagrange polynomials. Plane strain conditions are assumed.

Although the detailed results of the FE simulation can be found in Gouravaraju et al. [30, 77], for the sake of completeness, we briefly discuss the peeling process through a representative force-displacement plot. The entire peeling of the spatula can be divided into two phases based on the evolution of the normal and tangential pull-off forces shown in Fig. 2. In the first phase (from displacement  $\bar{u}^0$  to  $\bar{u}^{\text{max}}$ ), the spatula continuously undergoes stretching due to the fact that it is in a state of partial sliding/sticking near the peeling front. Thus, it accumulates strain energy. At  $\bar{u}^{\text{max}}$  the spatula is stretched to the maximum as the pull-off forces reach a maximum value. During the second phase (from  $\bar{u}^{\text{max}}$  to  $\bar{u}^{\text{det}}$ ) the spatula fully slides on the substrate. As a result, the spatula relaxes and releases the accumulated

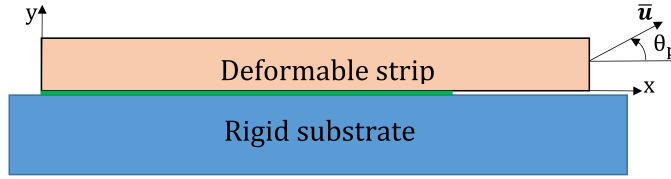


**Figure 1:** Peeling of a deformable strip from a rigid substrate. The strip is adhering on 75% of the surface.

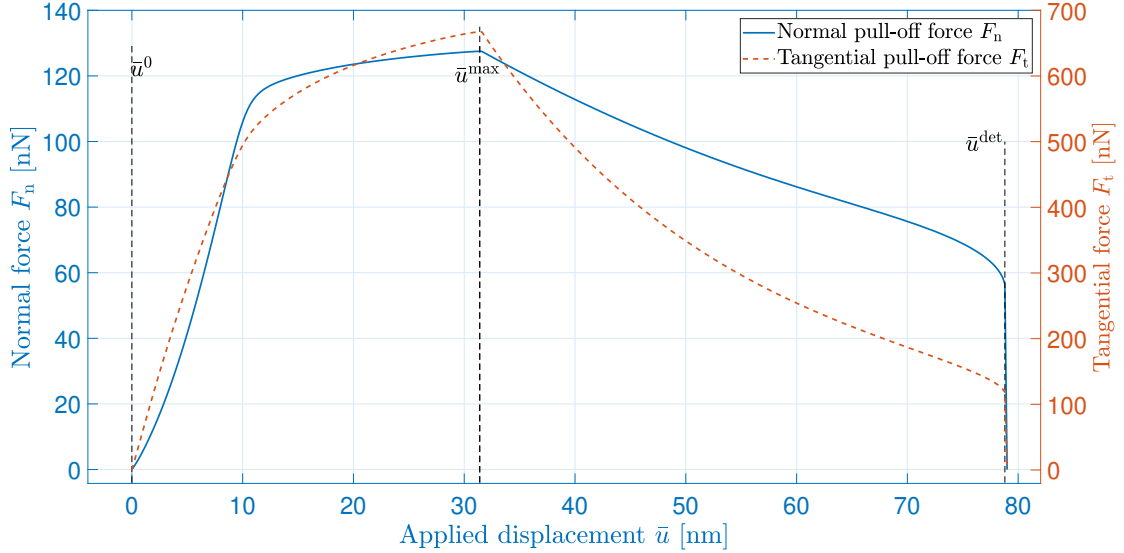


**Figure 2:** Evolution of normal ( $F_n$ ) and tangential ( $F_t$ ) pull-off forces with the applied displacement  $\bar{u}$  for peeling angle  $\theta_p = 45^\circ$ .

energy until it detaches from the substrate spontaneously at  $\bar{u}^{\text{det}}$ . Similar peeling curves are obtained for other peeling angles.

In this study, the focus is on three aspects of the peeling process viz. the maximum normal pull-off force  $F_n^{\text{max}}$ , the maximum tangential pull-off force  $F_t^{\text{max}}$ , and the resultant force angle  $\alpha = \arctan(F_n/F_t)$  at detachment. It has been shown that depending on the peeling angle  $\theta_p$ , the maximum pull-off forces  $F_n^{\text{max}}$  and  $F_t^{\text{max}}$ , the corresponding displacement  $\bar{u}^{\text{max}}$  and the detachment displacement  $\bar{u}^{\text{det}}$  vary considerably [30]. On the other hand, it has been observed [30, 77] that the resultant force angle at detachment  $\alpha^{\text{det}}$  remains the same irrespective of the peeling angle (see Table A1 in Appendix 1).

### 3. Bayesian regularization-backpropagation neural network (BR-BPNN)

In this section, a backpropagation neural network (BPNN) along with the Bayesian regularization learning algorithm are described.

A classical neural network architecture mimics the function of the human brain. The brain neurons and their connections with each other form an equivalence relation with neural network neurons and their associated weight values ( $w$ ). In a single layer network with multiple neurons, each element  $u_j$  of an input vector is associated with each neuron  $i$  with a corresponding weight  $w_{ij}$ . A constant scalar term called bias  $b_i$  corresponding to each neuron, which is like a weight, is generally introduced in order to increase the flexibility of the network. This bias  $b_i$  is multiplied by a scalar input value (chosen to be 1 here) and is added to the weighted sum  $w_{ij}u_j$  of the vector components  $u_j$  to form a net input  $n_i$ . This net input  $n_i$  is then passed to an activation function  $f$  (also called transfer function) that produces an output value  $a_i$ . In general, a neural network consists of two or more layers. Adding a hidden layer of neurons

between the input layer and output layer constitutes a multi-layer neural network, also named shallow neural network. Furthermore, addition of more than one hidden layer in the multi-layer neural network is called a deep neural network.

Traditionally, a BPNN model, a kind of multi-layer neural network, comprises three layers: an input layer, one or more hidden layers, and an output layer, as shown in Fig. 3. The input layer associates the input vector  $\mathbf{u}$  having  $R$  elements with input weight matrix  $\mathbf{W}^1$  and first bias vector  $\mathbf{b}^1$  to yield an effective input  $\mathbf{n}^1$  to the activation function  $\mathbf{f}^1$ , which produces an output vector  $\mathbf{a}^1$ . The output vector  $\mathbf{a}^1$  from the first layer forms the input to the hidden layer and is associated with the weight matrix  $\mathbf{W}^2$  and bias vector  $\mathbf{b}^2$  of the hidden layer. At last, the hidden layer output  $\mathbf{a}^2$  is given as an input to the output layer and delivers a predicted output  $\mathbf{a}^3$  with weight matrix  $\mathbf{W}^3$  and bias vector  $\mathbf{b}^3$ . In a neural network with a total of  $n_l$  number of layers, the weight matrix  $\mathbf{W}^l$  and bias vector  $\mathbf{b}^l$  for layer  $l$  (where  $l = 1, 2, \dots, n_l$ ) can be written as

$$\mathbf{W}^l = \begin{bmatrix} w_{11}^l & w_{12}^l & w_{13}^l & \dots & w_{1R}^l \\ w_{21}^l & w_{22}^l & w_{23}^l & \dots & w_{2R}^l \\ \vdots & \vdots & \vdots & \ddots & \vdots \\ w_{N^l 1}^l & w_{N^l 2}^l & w_{N^l 3}^l & \dots & w_{N^l R}^l \end{bmatrix}, \quad \mathbf{b}^l = \begin{bmatrix} b_1^l \\ b_2^l \\ \vdots \\ b_{N^l}^l \end{bmatrix}, \quad (5)$$

where  $N^l$  denotes the number of neurons in layer  $l$  and the effective input  $\mathbf{n}^l$  is then given as

$$\mathbf{n}^l = \mathbf{W}^l \mathbf{a}^{l-1} + \mathbf{b}^l, \quad \text{with } \mathbf{a}^0 = \mathbf{u}. \quad (6)$$

The number of neurons in the input layer ( $N^1$ ) and output layer ( $N^3$ ) is linked to the number of input and output vectors, respectively. However, the number of neurons in the hidden layer ( $N^2$ ) are accountable for the quantification of the weights and biases. The optimal network structure is versed by the optimum number of neurons in each layer required for the training and denoted as  $N^1$ - $N^2$ - $N^3$ . A variety of activation functions are used in backpropagation neural network viz., hard limit, linear, sigmoid, log-sigmoid, hyperbolic tangent sigmoid [83]. In the current work, linear activation functions are employed in all the layers according to which, the output is equal to the input i.e.  $\mathbf{a}^l = \mathbf{n}^l$ .

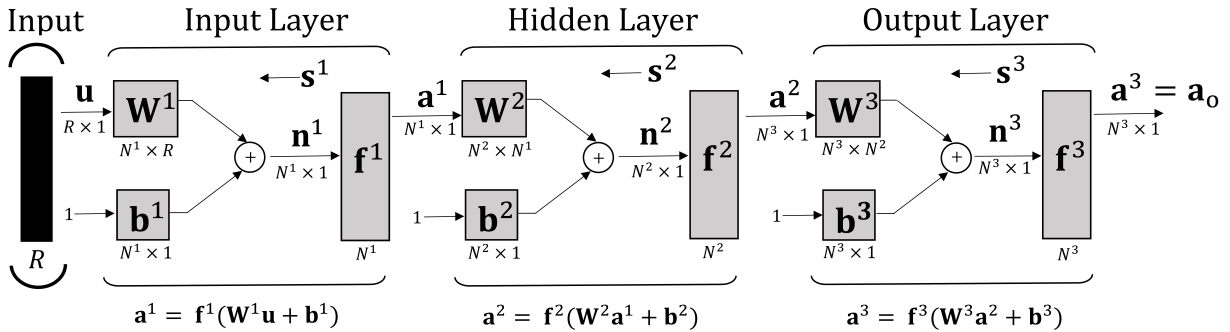


Figure 3: A typical backpropagation neural network with input, hidden, and output layers. Adapted from [83].

The network error  $\mathbf{e}$  is calculated by subtracting predicted output  $\mathbf{a}_o$  from target output  $\mathbf{t}_o$ . The sensitivity  $\mathbf{s}$ , i.e. the measure of how the output of the network changes due to perturbations in the input, is back-propagated from output layer ( $\mathbf{s}^3$ ) to input layer ( $\mathbf{s}^1$ ) via the hidden layer ( $\mathbf{s}^2$ ). Through the backpropagation process, the error of the neurons in the hidden layer is estimated as the backward weighted sum of the sensitivity. Thereafter, to update weights, different learning algorithms are used in association with the sensitivity such as the steepest descent, LM, and conjugate gradient algorithms. The sensitivity at layer  $l$  is calculated using the recurrence relation [83]

$$\mathbf{s}^l = \dot{\mathbf{F}}^l(\mathbf{n}^l) \mathbf{W}^{l+1} \mathbf{s}^{l+1}, \quad \text{where } l = n_l - 1, \dots, 2, 1, \quad (7)$$

$$\text{with } \mathbf{s}^{n_l} = \dot{\mathbf{F}}^{n_l}(\mathbf{n}^{n_l}) (\mathbf{t}_o - \mathbf{a}_o), \quad (8)$$

where  $\dot{\mathbf{F}}^l(\mathbf{n}^l)$  is a diagonal matrix containing the partial derivatives of the activation function  $\mathbf{f}^l$  with respect to the net inputs  $\mathbf{n}^l$  and is given as

$$\dot{\mathbf{F}}^l(\mathbf{n}^l) = \begin{bmatrix} f^l(n_1^l) & 0 & \dots & 0 \\ 0 & f^l(n_2^l) & \dots & 0 \\ \vdots & \vdots & \ddots & \vdots \\ 0 & 0 & \dots & f^l(n_{N^l}^l) \end{bmatrix}, \quad \text{where } f^l(n_j^l) = \frac{\partial f^l(n_j^l)}{\partial n_j^l}, \quad (9)$$

and for the considered linear activation function is equal to the identity matrix.

The purpose of a backpropagation neural network model is to ensure a network with small deviations for the training dataset and supervise the unknown inputs effectively. The intricacy of the BPNN, monitored by neurons in the hidden layer and their associated weights, leads to overfitting, i.e. the network tries to make the error as small as possible for the training set but performs poorly when new data is presented. However, a robust network model should be able to generalize well, i.e. it should predict well even when presented with new data. Therefore, Bayesian regularization based learning of BPNN models is utilized to achieve better generalization and minimal over-fitting for the trained networks [67, 68].

Consider a neural network with training dataset  $D$  having  $n_t$  number of input  $\mathbf{u}$  and target  $\mathbf{t}_o$  vector pairs in the network model, i.e

$$D = \left\{ (\mathbf{u}_1, \mathbf{t}_{o1}), (\mathbf{u}_2, \mathbf{t}_{o2}), \dots, (\mathbf{u}_{n_t}, \mathbf{t}_{on_t}) \right\}. \quad (10)$$

For each input to the network, the difference between target output ( $\mathbf{t}_o$ ) and predicted output ( $\mathbf{a}_o$ ) is computed as error  $\mathbf{e}$ . In order to evaluate the performance of the network, i.e. how well the neural network is fitting the test data, a quantitative measure is needed. This measure is called performance index of the network and is used to optimize the network parameters. The standard performance index  $F(\bar{\mathbf{w}})$  is governed by the sum of the squared errors (SSE)

$$F(\bar{\mathbf{w}}) = E_D = \sum_{i=1}^{n_t} (\mathbf{e}_i)^2 = \sum_{i=1}^{n_t} (\mathbf{t}_{oi} - \mathbf{a}_{oi})^T (\mathbf{t}_{oi} - \mathbf{a}_{oi}), \quad (11)$$

where  $\bar{\mathbf{w}}$  denotes the vector of size  $K$  containing all the weights and biases of the network

$$\bar{\mathbf{w}}^T = [\mathbf{w}^1, \mathbf{w}^2, \dots, \mathbf{w}^{n_t}]_{1 \times K}, \quad (12)$$

where

$$K = N^1(R+1) + N^2(N^1+1) + \dots + N^{n_t}(N^{n_t-1}+1), \quad (13)$$

and

$$(\mathbf{w}^l)^T = [w_{11}^l, w_{12}^l, \dots, w_{N^1 R}^l, b_1^l, b_2^l, \dots, b_{N^l}^l]. \quad (14)$$

As described in the introduction, in order to generalize the neural network, the performance index of Eq. (11) is modified using a regularization method. A penalty term  $(\mu/\nu)E_w$  is added to the performance index  $F(\bar{\mathbf{w}})$  [84],

$$F(\bar{\mathbf{w}}) = \mu E_w + \nu E_D, \quad (15)$$

where  $\mu$  and  $\nu$  are the regularization parameters and  $E_w$  represents the sum of the squared network weights (SSW), i.e.

$$E_w = \bar{\mathbf{w}}^T \bar{\mathbf{w}}. \quad (16)$$

Finding the optimum values for  $\mu$  and  $\nu$  is a challenging task, as their comparative values set up the basis for the training error. If  $\mu \ll \nu$ , smaller errors are generated, while if  $\mu \gg \nu$ , there should be reduced weight size at the cost of network errors [70]. For the purpose of finding the optimum regularization parameters, a Bayesian regularization method is employed.

Considering the network weights  $\bar{\mathbf{w}}$  as random variables, the aim is to choose the weights that maximize the posterior probability distribution of the weights  $P(\bar{\mathbf{w}}|D, \mu, \nu, M_N)$  given a certain data  $D$ . According to Bayes' rule [67], the posterior distribution of the weights depends on the likelihood function  $P(D|\bar{\mathbf{w}}, \nu, M_N)$ , the prior density  $P(\bar{\mathbf{w}}|\mu, M_N)$ , and the normalization factor  $P(D|\mu, \nu, M_N)$  for a particular neural network model  $M_N$  and can be evaluated from

$$P(\bar{\mathbf{w}}|D, \mu, \nu, M_N) = \frac{P(D|\bar{\mathbf{w}}, \nu, M_N) P(\bar{\mathbf{w}}|\mu, M_N)}{P(D|\mu, \nu, M_N)}. \quad (17)$$

Considering that the noise in the training set has a Gaussian distribution, the likelihood function is given by

$$P(D|\bar{\mathbf{w}}, \nu, M_N) = \frac{\exp(-\nu E_D)}{Z_D(\nu)}, \quad (18)$$

where  $Z_D = (\pi/\nu)^{Q/2}$  and  $Q = n_t \times N^{n_l}$ .

Similarly, assuming a Gaussian distribution for the network weights, the prior probability density  $P(\bar{\mathbf{w}}|\mu, M_N)$  is given as

$$P(\bar{\mathbf{w}}|\mu, M_N) = \frac{\exp(-\mu E_w)}{Z_w(\mu)}, \quad (19)$$

where  $Z_w = (\pi/\alpha)^{K/2}$ .

The posterior probability with the network weights  $\bar{\mathbf{w}}$  can then be expressed as [70]

$$P(\bar{\mathbf{w}}|D, \mu, \nu, M_N) = \frac{\exp(-\mu E_w - \nu E_D)}{Z_F(\mu, \nu)} = \frac{\exp(-F(\bar{\mathbf{w}}))}{Z_F(\mu, \nu)}, \quad (20)$$

where  $Z_F(\mu, \nu) = Z_D(\nu) Z_w(\mu)$  is the normalization factor.

The complexity of the model  $M_N$  is governed by regularization parameters  $\mu$  and  $\nu$ , which need to be estimated from the data. Therefore, Bayes' rule is again applied to optimize them as follows:

$$P(\mu, \nu|D, M_N) = \frac{P(D|\mu, \nu, M_N) P(\mu, \nu|M_N)}{P(D|M_N)}, \quad (21)$$

where  $P(\mu, \nu|M_N)$  denotes the assumed uniform prior density for the parameters  $\mu$  and  $\nu$ . From Eq. (21), it is evident that maximizing the likelihood function  $P(D|\mu, \nu, M_N)$  eventually maximizes the posterior probability  $P(\mu, \nu|D, M_N)$ . Moreover, it can be noted that the likelihood function in Eq. (21) is the normalization factor of Eq. (17). Therefore, solving for the likelihood function  $P(D|\mu, \nu, M_N)$  and expanding the objective function in Eq. (15) around the minimal point  $\bar{\mathbf{w}}^*$  via a Taylor series expansion, the optimum values of regularization parameters can be evaluated as follows [85]

$$\mu^* = \frac{\gamma}{2E_w(\bar{\mathbf{w}}^*)} \quad \text{and} \quad \nu^* = \frac{Q - \gamma}{2E_D(\bar{\mathbf{w}}^*)}, \quad (22)$$

where  $\gamma$  signifies the "number" of effective parameters exhausted in minimizing the error function

$$\gamma = K - \mu^* \text{tr}(\mathbf{H}^*)^{-1}, \quad \text{for } 0 \leq \gamma \leq K, \quad (23)$$

and  $\mathbf{H}^*$  is the Hessian matrix of the objective function evaluated at  $\bar{\mathbf{w}}^*$  and is calculated using the Gauss-Newton approximation as [70]

$$\mathbf{H}^* \approx \mathbf{J}^T \mathbf{J}, \quad (24)$$

where  $\mathbf{J}$  is the Jacobian matrix formed by the first derivatives of the network errors  $\mathbf{e}$  with respect to network weights  $w_{ij}$ . In (23),  $\text{tr}(\cdot)$  denotes the trace operator. The normalization factor  $Z_F(\mu, \nu)$  can then be approximated as [83]

$$Z_F(\mu, \nu) \approx (2\pi)^{K/2} (\det(\mathbf{H}^*))^{-1/2} \exp(-F(\bar{\mathbf{w}}^*)). \quad (25)$$

At the end of the training, a few checks regarding the number of effective parameters are required for better performance of the network [70]. The problem of computing the Hessian matrix at the minimal point  $\bar{\mathbf{w}}^*$  is implicitly solved in the Levenberg-Marquardt (LM) training algorithm while finding the minimum of  $F(\bar{\mathbf{w}})$ . In the LM algorithm, the network weights and biases at the  $k^{\text{th}}$  iteration are adjusted according to [67, 85]

$$\bar{\mathbf{w}}^{k+1} = \bar{\mathbf{w}}^k - [\mathbf{J}^T \mathbf{J} + \lambda \mathbf{I}]^{-1} \mathbf{J}^T \mathbf{e}, \quad (26)$$

where  $\lambda$  denotes the Levenberg's damping factor and  $\mathbf{J}^T \mathbf{e}$  is the error gradient, which needs to be close to zero at end of the training.

#### 4. Implementation of BR-BPNN

In this work, the input vector  $\mathbf{u}$  of the BR-BPNN models contains seventeen elements with peeling angle values  $\theta_p$  ranging from  $10^\circ$  to  $90^\circ$  at an interval of  $5^\circ$ . The corresponding output vectors are the maximum normal pull-off force  $F_n^{\max}$ , the maximum tangential pull-off force  $F_t^{\max}$ , the applied displacement at force maximum  $\bar{\mathbf{u}}^{\max}$ , the resultant force angle at detachment  $\alpha^{\text{det}}$ , and the applied displacement at detachment  $\bar{\mathbf{u}}^{\text{det}}$ . In general, this input-output dataset is randomly divided into training, validation, and testing sub-datasets. The training dataset is used to train the neural network model (which in the current work is carried out using the Bayesian regularization-backpropagation method) and the trained model is further validated with the validation dataset. The validation dataset, in other backpropagation training algorithms, is used to optimize the hyperparameters for effective training. The hyperparameters, like the number of neurons in the hidden layer and the learning parameters such as  $\gamma$  and  $\lambda$ , are defined as the variables required for training the neural network. However, for BR based learning networks, the hyperparameters in the form of the regularization parameters  $(\mu, \nu)$  are implicitly optimized using Eq. (15). Therefore, the validation set is not essentially required in this case for optimizing the network hyperparameters. Finally, the testing dataset (or sometimes called unseen dataset) is utilized to predict the target output  $\mathbf{t}_0$  and analyze the model performance, accordingly.

As described previously, the neural network model is first trained on the training dataset and its performance is evaluated by making predictions using the testing dataset. However, this type of single-run model-validation method could potentially result in selection-bias, i.e. the accuracy of the model will be highly dependent on the particular choice of the training and testing datasets. In order to assess the effectiveness of a neural network model developed using limited data, as in this work, a cross-validation method called  $k$ -fold cross-validation method is employed in the training of neural networks. This helps the neural network to generalize to new or unseen data in a much better manner. In the  $k$ -fold cross-validation method the complete dataset is divided into two complementary sub-datasets, i.e. training and testing. In this method, for a given neural network model, the dataset is first randomized and then partitioned (split) into a  $k$  number of almost equal sized sub-datasets called folds. Then, the  $k - 1$  folds are used to train the neural network. The one remaining fold (i.e.,  $k^{\text{th}}$  fold) is used for testing the performance of the neural network model. This process is repeated  $k$  times such that the network is trained and tested on the entire dataset as illustrated in Table 1 which shows the dataset split five times (Split 1 to Split 5) into five folds (Fold 1 to Fold 5). The yellow cells in Table 1 represent testing dataset while the blue cells correspond to training dataset. The performance of the neural network is then reported in terms of the average accuracy obtained from this  $k$ -fold cross-validation.

Table 2 give the details of testing dataset and testing dataset used in  $k$ -fold cross-validation. The indices in the table refer to the case number in Table A1 (first column). For each split, the training dataset is used to train the neural network model using Bayesian regularization method and the trained model is further validated with the validation dataset using the fold mentioned in the last column of Table 2. The validation dataset, in other back-propagation training algorithms, is used to optimize the hyperparameters for effective training. The hyperparameters, like the number of neurons in the

**Table 1**

K-fold cross-validation with dataset split into five folds. The yellow cells represent testing dataset while the blue cells correspond to training dataset. See Table 2 for explicit details for the folds used in the present work.

<b>Split 1</b>	Fold 1	Fold 2	Fold 3	Fold 4	Fold 5
<b>Split 2</b>	Fold 1	Fold 2	Fold 3	Fold 4	Fold 5
<b>Split 3</b>	Fold 1	Fold 2	Fold 3	Fold 4	Fold 5
<b>Split 4</b>	Fold 1	Fold 2	Fold 3	Fold 4	Fold 5
<b>Split 5</b>	Fold 1	Fold 2	Fold 3	Fold 4	Fold 5

**Table 2**

Details of training dataset and testing dataset used in the  $k$ -fold cross-validation. The indices refer to the case number (first column) in Table A1.

Split Number	Training dataset indices	Number of training data ( $N_{\text{train}}$ )	Testing dataset indices	Number of testing data ( $N_{\text{test}}$ )	Fold for Testing dataset
<b>Split 1</b>	1, 2, 5, 6, 8, 10, 11, 12, 13, 14, 15, 16, 17	13	3, 4, 7, 9	4	Fold 1
<b>Split 2</b>	1, 2, 3, 4, 5, 6, 7, 8, 9, 10, 11, 11, 14, 15, 16	14	12, 13, 17	3	Fold 2
<b>Split 3</b>	2, 3, 4, 5, 7, 8, 9, 12, 13, 14, 15, 16, 17	13	1, 6, 10, 11	4	Fold 3
<b>Split 4</b>	1, 3, 4, 5, 6, 7, 9, 10, 11, 12, 13, 15, 16, 17	14	2, 8, 14	3	Fold 4
<b>Split 5</b>	1, 2, 3, 4, 4, 6, 7, 8, 9, 10, 11, 12, 13, 14, 17	14	5, 15, 16	3	Fold 5

hidden layer and the learning parameters such as  $\gamma$  and  $\lambda$ , are defined as the variables required for training the neural network. However, for BR based learning networks, the hyperparameters in the form of the regularization parameters ( $\mu, \nu$ ) are implicitly optimized using Eq. (15). Therefore, the validation set is not essentially required in this case for optimizing the network hyperparameters. Finally, the testing dataset is utilized to predict the targeted output  $\mathbf{t}_0$  and analyze the model performance, accordingly. Appendix B presents a simple algorithmic overview of BR-BPNN model developed in the present work.

Next, two BR-BPNN models are formed with different output datasets; the first model has three output vectors and the second model has two output vectors as shown in Table 3. The three output vectors for BR-BPNN-I are the applied displacement at force maximum  $\bar{\mathbf{u}}^{\text{max}}$ , the maximum normal pull-off force  $F_n^{\text{max}}$ , and the maximum tangential pull-off force  $F_t^{\text{max}}$ . For BR-BPNN-II, the output vectors are the applied displacement at detachment  $\bar{\mathbf{u}}^{\text{det}}$  and the resultant force angle at detachment  $\alpha^{\text{det}}$ , respectively. Each output vector consists of  $3N_{\text{test}}$  and  $2N_{\text{test}}$  elements for BPNN-I and BPNN-II models respectively.

However, only  $N_{\text{train}}$  elements corresponding to the input training dataset (see Table 2) are selected for training the BPNN models. Then, the input and output vectors are normalized by the corresponding maximum values. The performance of BR-BPNN models are estimated by comparing the MSE values with the number of neurons in the hidden layer and determining the optimal number. The MSE is computed using the network error and defined as the mean of the sum of squared networks errors, i.e.

$$\text{MSE} = \frac{1}{n_t} E_D. \quad (27)$$

## 5. Results and discussion

This section presents the Bayesian regularization-based backpropagation neural network predictions of the maximum normal pull-off force  $F_n^{\text{max}}$ , the maximum tangential pull-off force  $F_t^{\text{max}}$ , and the resultant force angle at detachment  $\alpha^{\text{det}}$  along with the corresponding displacements  $\bar{\mathbf{u}}^{\text{max}}$  and  $\bar{\mathbf{u}}^{\text{det}}$ . Predictions of the networks are then compared

**Table 3**

Output dataset for two different BR-BPNN models (see Appendix A for the FE results).

BR-BPNN-I	
Applied displacement at force maximum	$\bar{\mathbf{u}}^{\max} := [\bar{u}_1^{\max}, \bar{u}_2^{\max}, \dots, \bar{u}_{16}^{\max}, \bar{u}_{17}^{\max}]^T$
Maximum normal pull-off force	$\mathbf{F}_n^{\max} := [F_{n_1}^{\max}, F_{n_2}^{\max}, \dots, F_{n_{16}}^{\max}, F_{n_{17}}^{\max}]^T$
Maximum tangential pull-off force	$\mathbf{F}_t^{\max} := [F_{t_1}^{\max}, F_{t_2}^{\max}, \dots, F_{t_{16}}^{\max}, F_{t_{17}}^{\max}]^T$
BR-BPNN-II	
Applied displacement at detachment	$\bar{\mathbf{u}}^{\det} := [\bar{u}_1^{\det}, \bar{u}_2^{\det}, \dots, \bar{u}_{16}^{\det}, \bar{u}_{17}^{\det}]^T$
Resultant force angle at detachment	$\boldsymbol{\alpha}^{\det} := [\alpha_1^{\det}, \alpha_2^{\det}, \dots, \alpha_{16}^{\det}, \alpha_{17}^{\det}]^T$

with the FE results of Gouravaraju et al. [30, 77] that have not been yet used for training.

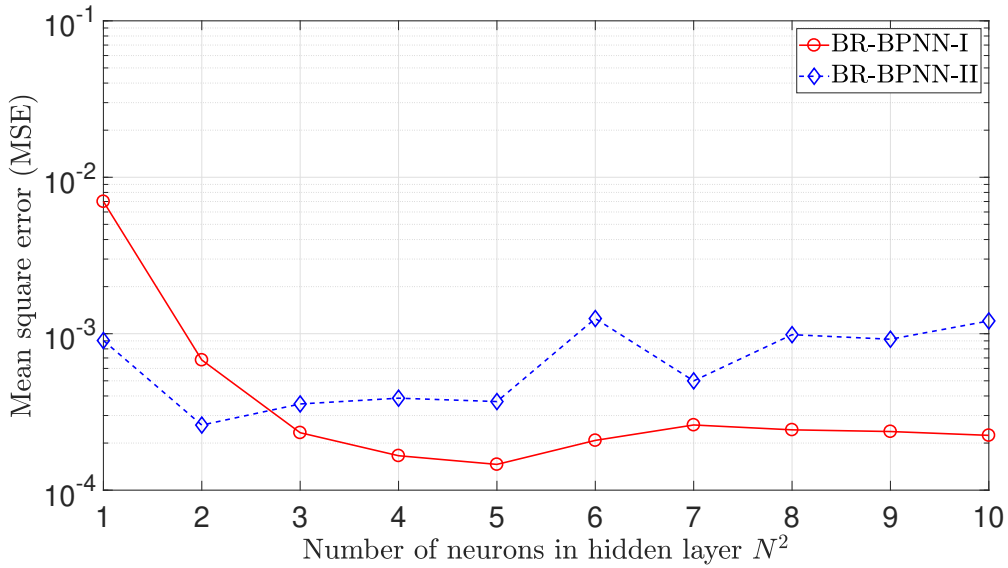


**Figure 4:** Average Mean square error from 5-fold cross-validation vs. number of neurons in the hidden layer for different BR-BPNN models.

To define the optimal structure of each network model, the mean square error (MSE) of Eq. (27) is investigated along with the number of neurons (1 to 10) in the hidden layer. For the two BR-BPNN models (BR-BPNN-I and BR-BPNN-II), training is performed with 1 to 10 hidden neurons. The MSE values for both the models with only one hidden neuron are found to be comparatively high i.e.  $7 \times 10^{-3}$  and  $9.045 \times 10^{-4}$ , being incapable to form an efficient network. However, as the number of hidden neurons increases to two, a major drop in the MSE values ( $6.793 \times 10^{-4}$ , and  $2.6060 \times 10^{-4}$ ) is recorded. Each model is trained 15 times independently for different number of neurons to mitigate the unfavorable effects by choosing random initial weights. Each network model is trained for a maximum of 2000 epochs. An epoch is completed when the entire training dataset is passed forward and backward through the network thus updating the weights once. For the BPNN-I, the mean square error attains a broad minimum and continuous to decrease between 1 and 5 hidden neurons as shown in Fig. 4. For  $N^2$  greater than 5, the MSE value again starts to rise due to overfitting of the network models. Therefore, for BPNN-I the number of neurons in the hidden layer is selected as 5. The number of neurons in the input and output layers are taken as 1 and 3 as there is one input vector and three output vectors for BPNN-I model. Following a similar trend, the optimal number of hidden neurons for BPNN-II model is found to be 2, forming the network structure 1-2-2.

Either of the following criteria are selected to terminate or complete the training process: maximum number of

epochs reached, minimum value of performance gradient reached, minimum constant value of effective parameters ( $\gamma$ ) reached, maximum value of Levenberg's damping factor ( $\lambda$ ) attained, or MSE reached within the performance limits. The training results for BR-BPNN-I and BR-BPNN-II models are shown in Tables 4 and 5 respectively. The other network training parameters like the sum of square errors (SSE) (Eq. (11)), sum of square weights (SSW) (Eq. (16)), Levenberg's damping factor, and error gradient (Eq. (26)) values are also shown in Tables 4 and 5.

**Table 4**

Training parameters for best configuration (1-5-3) for BR-BPNN-I from 5-fold cross validation.

	Epochs	MSE	SSE( $E_D$ )	SSW ( $E_W$ )	No. of effective parameters ( $\gamma$ )	LM Parameter ( $\lambda$ )	Gradient ( $\mathbf{J}^T \mathbf{e}$ )
Split 1	384	$9.79 \times 10^{-04}$	$3.26 \times 10^{-04}$	63.98	22.18	1.0	$9.88 \times 10^{-08}$
Split 2	300	$7.39 \times 10^{-05}$	$2.47 \times 10^{-05}$	80.97	22.38	$1.0 \times 10^{10}$	$1.07 \times 10^{-07}$
Split 3	145	$2.36 \times 10^{-06}$	$7.81 \times 10^{-07}$	56.61	23.26	$1.0 \times 10^{10}$	$1.31 \times 10^{-07}$
Split 4	92	$1.86 \times 10^{-06}$	$6.21 \times 10^{-07}$	110.29	24.90	$1.0 \times 10^{10}$	$1.34 \times 10^{-07}$
Split 5	106	0.0011	$3.62 \times 10^{-04}$	46.91	23.15	1.0	$9.88 \times 10^{-08}$

**Table 5**

Training parameters for best configuration (1-2-2) for BR-BPNN-II from 5-fold cross validation.

	Epochs	MSE	SSE( $E_D$ )	SSW ( $E_W$ )	No. of effective parameters ( $\gamma$ )	LM Parameter ( $\lambda$ )	Gradient ( $\mathbf{J}^T \mathbf{e}$ )
Split 1	64	$1.18 \times 10^{-05}$	$3.93 \times 10^{-06}$	53.71	8.57	$1.0 \times 10^{10}$	$4.23 \times 10^{-07}$
Split 2	82	$1.27 \times 10^{-05}$	$4.24 \times 10^{-06}$	60.20	8.26	$1.0 \times 10^{10}$	$5.76 \times 10^{-07}$
Split 3	43	$8.38 \times 10^{-06}$	$2.79 \times 10^{-06}$	37.29	8.31	$1.0 \times 10^{10}$	$7.75 \times 10^{-07}$
Split 4	68	$5.84 \times 10^{-06}$	$1.95 \times 10^{-06}$	43.26	8.51	$1.0 \times 10^{10}$	$8.93 \times 10^{-07}$
Split 5	115	$8.94 \times 10^{-06}$	$2.98 \times 10^{-06}$	62.13	8.43	$1.0 \times 10^{10}$	$7.59 \times 10^{-07}$

After training the models with input-output datasets with  $N_{\text{train}}$  datapoints (see Table 2), the testing dataset with  $N_{\text{test}}$  datapoints (see Table 2) is utilized to predict the corresponding desired output values. The relative error (RE) is used to measure the accuracy of the network predictions. The RE is calculated as the deviation of the predicted result from the desired target result, i.e.

$$\text{RE} = \frac{t_i - a_i}{t_i}, \quad (28)$$

where  $t_i$  and  $a_i$  denote the desired target result and the network prediction for a particular peeling angle of the testing data set, respectively.

### 5.1. Case I: Maximum normal and tangential pull-off forces

Based on the training parameters from Table 4, Figs. 5, 6, and 7 presents the predicted (BR-BPNN-I) results of the maximum normal pull-off force  $F_n^{\text{max}}$ , maximum tangential pull-off force  $F_t^{\text{max}}$  and the corresponding applied displacement  $\bar{u}^{\text{max}}$ . Since in the present work a 5-fold cross validation method is used the predicted and the desired results across all the splits is shown <sup>1</sup>. It can be seen from Figs. 5 and 6 that the predicted values of  $F_n^{\text{max}}$  and  $F_t^{\text{max}}$  for all angles except  $\theta_p = 10^\circ$  are very close to the desired target results (that are obtained by FE). However, for  $\theta_p = 10^\circ$ , the predicted results show slightly more deviation compared to the other tested peeling angles. The predictions are a little different for  $\bar{u}^{\text{max}}$  as shown in Fig. 7 where significant difference is found for  $\theta_p = 10^\circ, 20^\circ$ , and  $90^\circ$ . This can also be observed from Table 6, which lists the relative error (RE) for the all the tested peeling angles. From the table it can be seen that the maximum relative error for the case of displacement is 9.68% while the average relative error is around 1.22%. The average relative error for the case of maximum normal and tangential forces is found to be very small.

<sup>1</sup>The correlation between the split and the predicted indices can be found in Table 2

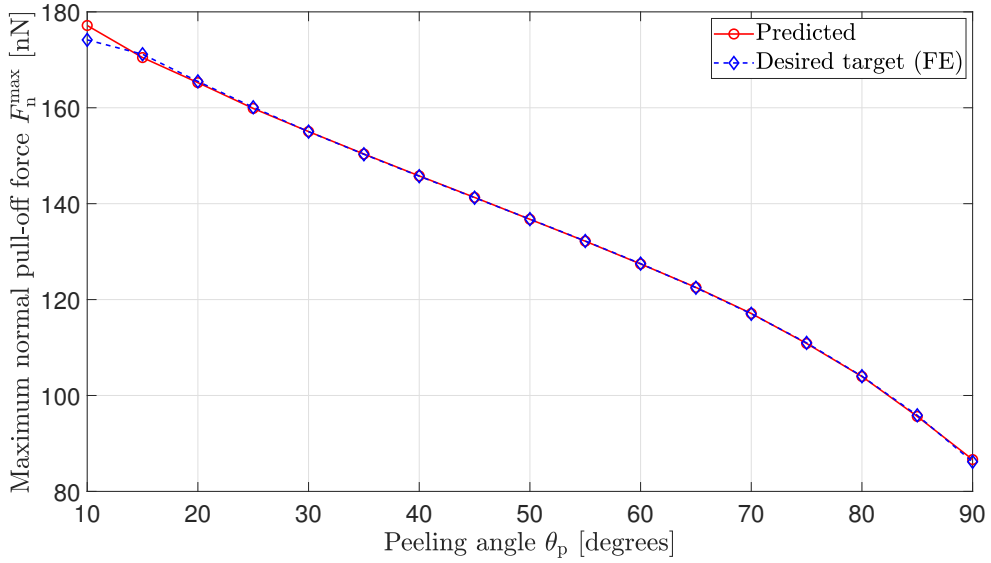


**Figure 5:** Plot of predicted and desired (FE) value of maximum normal pull-off force  $F_n^{\max}$  with the peeling angle  $\theta_p$  across all the splits for BR-BPNN-I model.

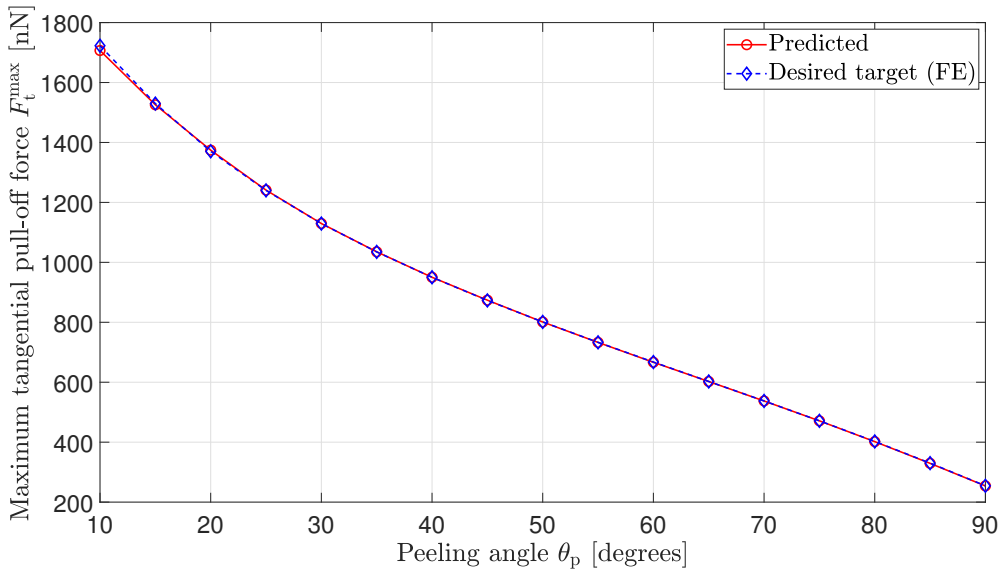


**Figure 6:** Plot of predicted and desired (FE) value of maximum tangential pull-off force  $F_t^{\max}$  with the peeling angle  $\theta_p$  across all the splits for BR-BPNN-I model.

### 5.2. Case II: Resultant force angle at detachment

Figures 8 and 9 show the predictions for the output dataset of BR-BPNN-II, i.e. the applied displacement at detachment  $\bar{u}^{\det}$  and the resultant force angle at detachment  $\alpha^{\det}$  using the corresponding training parameters from Table 5. Again, as mentioned previously, since in the present work a 5-fold cross validation method is used, the predicted and the desired results across all the splits is shown. It can be seen from Fig. 8 that the predicted values of  $\bar{u}^{\det}$  for all the angles except for  $\theta_p = 10^\circ$  are very close to the desired target FE results. The maximum, minimum and the average RE values, given in Table 7, are estimated to be 9.85%, 0.15%, and 1.24%, respectively. As shown in Fig. 9, the predicted values of  $\alpha^{\det}$  are also very close to the desired target FE results. The maximum, minimum and the average RE values corresponding to  $\alpha^{\det}$  predictions are estimated to be 0.66%, 0.06%, and 0.30%, respectively. It can be observed that the predictions are very accurate even outside of the training data set.

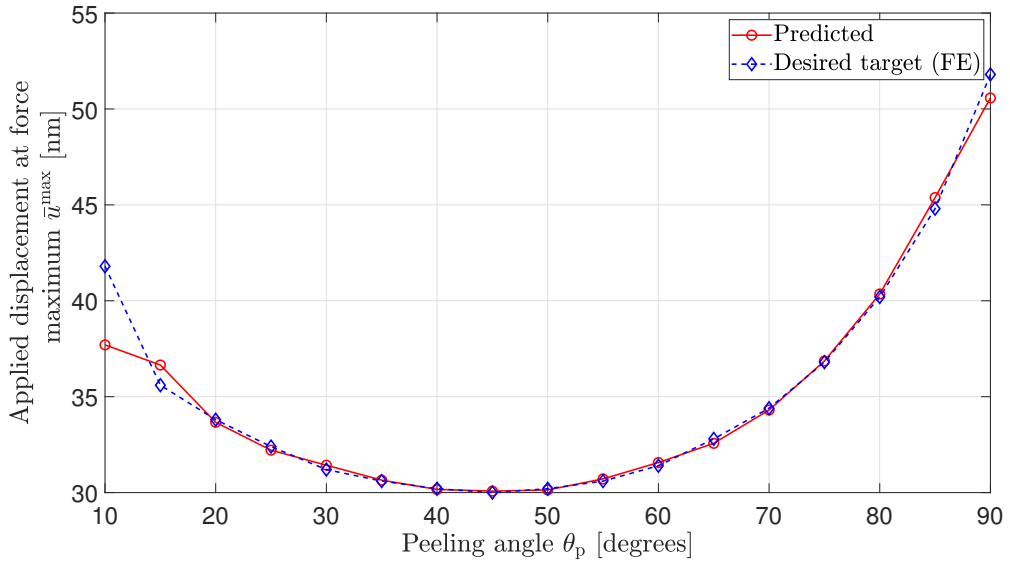


**Figure 7:** Plot of predicted and desired (FE) value of applied displacement  $\bar{u}^{\max}$  with the peeling angle  $\theta_p$  at maximum pull-off force across all the splits for BR-BPNN-I model.

**Table 6**

Relative error (RE) for the predictions of BR-BPNN-I model.

	$F_n^{\max}$	$F_t^{\max}$	$\bar{u}^{\max}$
Maximum RE (%)	1.78	0.91	9.68
Minimum RE (%)	$2.04 \times 10^{-4}$	0.0076	0.06
Average RE (%)	0.24	0.19	1.22

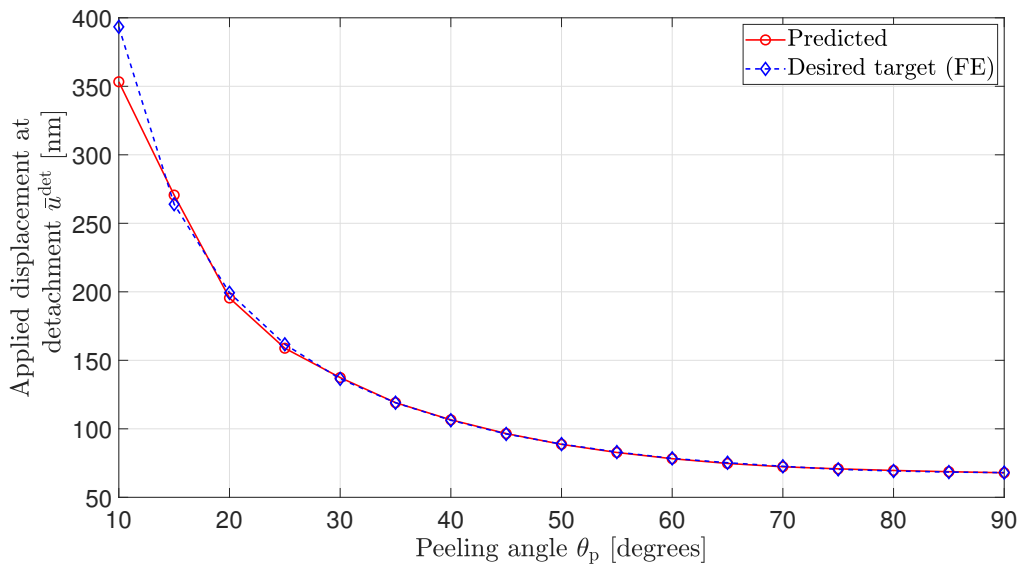


**Figure 8:** Plot of predicted and desired (FE) value of applied displacement at detachment  $\bar{u}^{\det}$  with the peeling angle  $\theta_p$  across all the splits for BR-BPNN-II model.

From all these results, it can be observed that for both the BR-BPNN models, the predictions are very close to the target outputs value except for  $\theta_p = 10^\circ$ . Further, for both the BR-BPNN-I and BR-BPNN-II models, the deviations

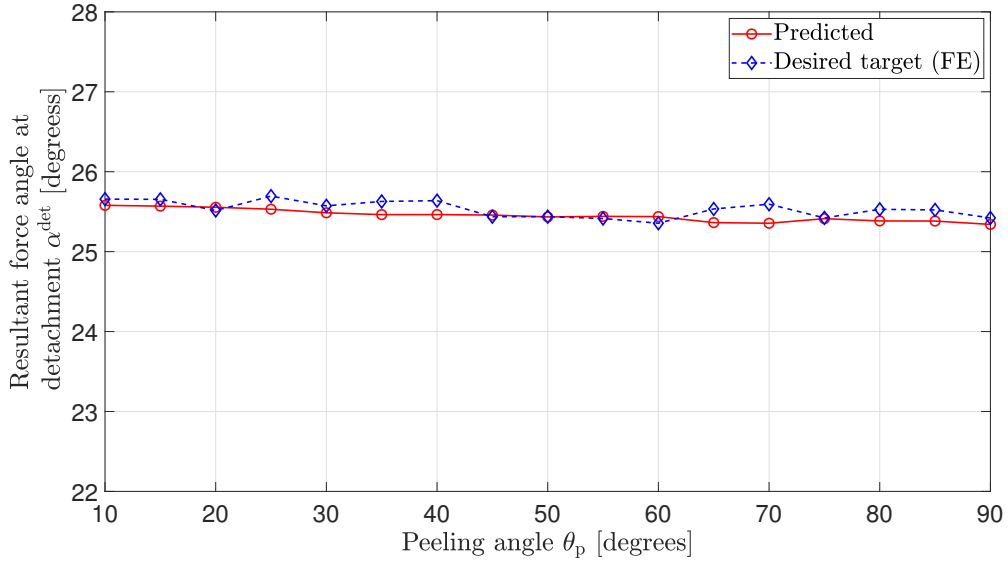


**Figure 9:** Plot of predicted and desired (FE) value of resultant force angle at detachment  $\alpha^{\det}$  with the peeling angle  $\theta_p$  across all the splits for BR-BPNN-II model

**Table 7**

Relative error (RE) for the predictions of BR-BPNN-III model.

	$\alpha^{\det}$	$\bar{u}^{\det}$
Maximum RE (%)	0.66	9.85
Minimum RE (%)	0.06	0.15
Average RE (%)	0.30	1.24

in the predictions are larger for displacements rather than forces. Whereas in case of BR- BPNN-I and BR-BPNN-II,  $\bar{u}^{\max}$ , and  $\bar{u}^{\det}$  vary quite abruptly near  $\theta_p = 10^\circ$ . This is because for both BR-BPNN-I and BR-BPNN-II,  $\bar{u}^{\max}$  and  $\bar{u}^{\det}$  vary quite abruptly at  $\theta_p = 10^\circ$  (as seen in Figures 7 and 8) and thus can be considered as outliers.

The important advantage of these ANN models lies in the significant reduction in computational cost. It is observed that the time to train the networks with the data corresponding to all the testing peeling angles of each split for both networks is hardly more than one minute. Similarly, once the network is trained, any number of predictions can be made within minutes. Thus, augmenting the FE models with ANNs can significantly reduce the computational time leading to faster analysis once the required data has been obtained. This gives a particularly big advantage when the data is obtained using experiments.

## 6. Conclusions

An artificial neural network model is constructed in the present work to study the peeling behavior of a thin strip such as a gecko spatula. In particular, the variation of the maximum normal and tangential pull-off forces, the corresponding applied displacement, the resultant force angle and the applied displacement at detachment as a function of the peeling angle are investigated. The input data is obtained from the finite element analysis of Gouravaraju et al. [30, 77]. Bayesian regularization in conjunction with k-fold cross validation method is used to form two separate networks. The two networks correspond to (a) the maximum normal and tangential pull-off force and the corresponding applied displacement, and (b) the resultant force angle and the applied displacement at detachment. The number of hidden neurons in each model are evaluated based on their respective mean square errors. From all the results, the maximum and minimum relative deviations of the predicted values from the FE results are found to be 9.85% and 0.0076%, respectively. Based on the results, it can be concluded that the Bayesian regularization-based backpropagation neural networks can be employed to successfully study peeling problems. The present work successfully confirms that augmenting the FE models with ANNs can significantly reduce the computational time in highly nonlinear FE

problems like the one investigated in the present work. Further, the proposed neural network models can be extended to predict the influence of various geometrical, material, and environmental factors on strip peeling. Another interesting problem that can be investigated using BR-BPNN is the constitutive modeling for the hierarchical structures in the gecko adhesion mechanism.

## A. Results from finite element simulations

Table A1 lists the values of the maximum normal force  $F_n^{\max}$ , maximum tangential force  $F_t^{\max}$ , applied displacement at force maximum  $\bar{u}^{\max}$ , applied displacement at  $\bar{u}^{\det}$ , and resultant force angle at detachment  $\alpha^{\det}$  for different peeling angles as obtained by Gouravaraju et al. [30, 77] using nonlinear finite element analysis.

Table A1: Data from finite element results of Gouravaraju et al. [30, 77].

Case	Peeling angle $\theta_p$ [degrees]	Applied displacement at force maximum $\bar{u}^{\max}$ [nm]	Maximum normal pull-off force $F_n^{\max}$ [nN]	Maximum tangential pull-off force $F_t^{\max}$ [nN]	Applied displacement at detachment $\bar{u}^{\det}$ [nm]	Resultant force angle at detachment $\alpha^{\det}$ [degrees]
1	10	41.8	174.1584	1722.719	393.4	25.64973
2	15	35.6	171.1613	1529.699	263.8	25.57726
3	20	33.8	165.5169	1370.545	199.6	25.56427
4	25	32.4	160.1255	1240.153	161.6	25.59890
5	30	31.2	155.0284	1129.391	136.6	25.60988
6	35	30.6	150.3356	1034.944	119.0	25.55115
7	40	30.2	145.7655	950.3074	106.2	25.55958
8	45	30.0	141.2537	872.9422	96.6	25.61840
9	50	30.2	136.8172	801.4117	89.2	25.65779
10	55	30.6	132.2554	733.2346	83.4	25.62680
11	60	31.4	127.5051	667.3803	78.8	25.53845
12	65	32.8	122.5176	602.7001	75.4	25.66338
13	70	34.4	117.0706	537.6730	72.6	25.51802
14	75	36.8	110.9777	471.2534	70.6	25.49363
15	80	40.2	104.0514	402.4569	69.4	25.69447
16	85	44.8	95.87533	330.1474	68.4	25.44845
17	90	51.8	86.18540	254.5306	68.2	25.49894

## B. Framework of Bayesian regularization-based backpropagation

The algorithm for the Bayesian regularization based backpropagation is composed of the following steps:

1. Pick training data set  $D$  containing the  $N_{\text{train}}$  cases specified in Table 2, 3, and Appendix A.
  - (a) Input vector,  $\mathbf{u}$ : Peeling angles  $\theta_p$
  - (b) Target output vector,  $\mathbf{t}_o$  :  $\bar{u}^{\max}$ ,  $F_n^{\max}$ ,  $F_t^{\max}$  (for BR-BPNN-I)  
 $\bar{u}^{\det}$ ,  $\alpha^{\det}$  (for BR-BPNN-II)
2. Initialize neural network with
  - (a) Number of neurons in the input layer equal to the number of input vectors, which is equal to 1 for both the BR-BPNN models as described in step 1(a), i.e.  $N^1 = 1$ .
  - (b) Number of neurons in the output layer equal to the number of output vectors, which is equal to  $N^3 = 3$  for BR-BPNN I and  $N^3 = 2$  for BR-BPNN II model respectively as described in Table 3.
  - (c) Number of neurons in the hidden layer equal to one, i.e.  $N^2 = 1$ .
3. Set learning method to Bayesian regularization
  - (a) Set maximum number of epochs to 2000.
  - (b) Divide the training data set as per Table 2 using  $k$ -fold cross validation.
4. Train the network

- (a) Compute regularization parameters  $\mu$  and  $\nu$  using Eq. (22).
  - (b) Backpropagate sensitivities calculated using Eqs. (7) and (8).
  - (c) Update weights using Eq. (26).
5. Compute mean square error (MSE) using Eq. (27).
  6. Loop over steps 4 and 5 with different number of neurons in the hidden layer.
  7. Plot the MSE with number of neurons in the hidden layer as in Fig. 4.
  8. Select the number of neurons in the hidden layer to be the value from which MSE attains a broad minimum and decreases as  $N^2$  is further increased. This determines the optimal network structure  $N^1-N^2-N^3$ .
  9. Retrain the neural network model with optimal network structure from step 8.
  10. Save the model parameters (using Tables 4 and 5) along with weights and biases.
  11. Using the saved parameters in step 10, predict for the testing dataset as in Tables 2 and 3.

## References

- [1] K. Komvopoulos. Adhesion and friction forces in microelectromechanical systems: mechanisms, measurement, surface modification techniques, and adhesion theory. *J. Adhes. Sci. Technol.*, 17(4):477–517, 2003. doi: 10.1163/15685610360554384.
- [2] X. Zhang, Y. Liu, Y. Liu, and S.I.-U. Ahmed. Controllable and switchable capillary adhesion mechanism for bio-adhesive pads: Effect of micro patterns. *Sci. Bull.*, 54(10):1648–1654, 2009. doi: 10.1007/s11434-009-0234-z.
- [3] M. Sexsmith and T. Troczynski. Peel adhesion test for thermal spray coatings. *J. Therm. Spray Technol.*, 3(4):404–411, 1994. doi: 10.1007/BF02658986.
- [4] C. Majidi, R.E. Groff, Y. Maeno, B. Schubert, S. Baek, B. Bush, R. Maboudian, N. Gravish, M. Wilkinson, K. Autumn, and R.S. Fearing. High Friction from a Stiff Polymer Using Microfiber Arrays. *Phys. Rev. Lett.*, 97(7):076103, 2006. doi: 10.1103/PhysRevLett.97.076103.
- [5] B. Schubert, C. Majidi, R.E. Groff, S. Baek, B. Bush, R. Maboudian, and R.S. Fearing. Towards friction and adhesion from high modulus microfiber arrays. *J. Adhes. Sci. Technol.*, 21(12-13):1297–1315, 2007. doi: 10.1163/156856107782328344.
- [6] D. Drotlef, M. Amjadi, M. Yunusa, and M. Sitti. Bioinspired Composite Microfibers for Skin Adhesion and Signal Amplification of Wearable Sensors. *Adv. Mater.*, 29(28):1701353, 2017. doi: 10.1002/adma.201701353.
- [7] C. Zhu. Kinetics and mechanics of cell adhesion. *J. Biomech.*, 33(1):23–33, 2000. doi: 10.1016/S0021-9290(99)00163-3.
- [8] B.N.J. Persson and S. Gorb. The effect of surface roughness on the adhesion of elastic plates with application to biological systems. *J. Chem. Phys.*, 119(21):11437–11444, 2003. doi: 10.1063/1.1621854.
- [9] R.A. Sauer. Multiscale modelling and simulation of the deformation and adhesion of a single gecko seta. *Comput. Methods Biomech. Biomed. Engin.*, 12(6):627–640, 2009. doi: 10.1080/10255840902802917.
- [10] D. Labonte and W. Federle. Biomechanics of shear-sensitive adhesion in climbing animals: peeling, pre-tension and sliding-induced changes in interface strength. *J. R. Soc. Interface*, 13(122):20160373, 2016. doi: 10.1098/rsif.2016.0373.
- [11] W. Federle and D. Labonte. Dynamic biological adhesion: mechanisms for controlling attachment during locomotion. *Philos. Trans. R. Soc. B Biol. Sci.*, 374(1784):20190199, 2019. doi: 10.1098/rstb.2019.0199.
- [12] Y. Tian, N. Pesika, H. Zeng, K. Rosenberg, B. Zhao, P. McGuiggan, K. Autumn, and J. Israelachvili. Adhesion and friction in gecko toe attachment and detachment. *Proc. Natl. Acad. Sci.*, 103(51):19320–19325, 2006. doi: 10.1073/pnas.0608841103.
- [13] N. S. Pesika, Y. Tian, B. Zhao, K. Rosenberg, H. Zeng, P. McGuiggan, K. Autumn, and J. N. Israelachvili. Peel-Zone Model of Tape Peeling Based on the Gecko Adhesive System. *J. Adhes.*, 83(4):383–401, 2007. doi: 10.1080/00218460701282539.
- [14] Z.L. Peng, S.H. Chen, and A.K. Soh. Peeling behavior of a bio-inspired nano-film on a substrate. *Int. J. Solids Struct.*, 47(14-15):1952–1960, 2010. doi: 10.1016/j.ijsolstr.2010.03.035.
- [15] R.A. Sauer. The Peeling Behavior of Thin Films with Finite Bending Stiffness and the Implications on Gecko Adhesion. *J. Adhes.*, 87(7-8): 624–643, 2011. doi: 10.1080/00218464.2011.596084.
- [16] K. Autumn, Y.A. Liang, S.T. Hsieh, W. Zesch, W.P. Chan, T.W. Kenny, R. Fearing, and R.J. Full. Adhesive force of a single gecko foot-hair. *Nature*, 405(6787):681–685, 2000. doi: 10.1038/35015073.
- [17] K. Takahashi, J.O.L. Berengueres, K.J. Obata, and S. Saito. Geckos' foot hair structure and their ability to hang from rough surfaces and move quickly. *Int. J. Adhes. Adhes.*, 26(8):639–643, 2006. doi: 10.1016/j.ijadhadh.2005.12.002.
- [18] B. Chen, P. Wu, and H. Gao. Pre-tension generates strongly reversible adhesion of a spatula pad on substrate. *J. R. Soc. Interface*, 6(35): 529–537, 2009. doi: 10.1098/rsif.2008.0322.
- [19] K. Autumn. Mechanisms of Adhesion in Geckos. *Integr. Comp. Biol.*, 42(6):1081–1090, 2002. doi: 10.1093/icb/42.6.1081.
- [20] G. Huber, S.N. Gorb, R. Spolenak, and E. Arzt. Resolving the nanoscale adhesion of individual gecko spatulae by atomic force microscopy. *Biol. Lett.*, 1(1):2–4, 2005. doi: 10.1098/rsbl.2004.0254.
- [21] W. Sun, P. Neuzil, T.S. Kustandi, S. Oh, and V.D. Samper. The Nature of the Gecko Lizard Adhesive Force. *Biophys. J.*, 89(2):L14–L17, 2005. doi: 10.1529/biophysj.105.065268.
- [22] H. Gao, X. Wang, H. Yao, S. Gorb, and E. Arzt. Mechanics of hierarchical adhesion structures of geckos. *Mech. Mater.*, 37(2-3):275–285, 2005. doi: 10.1016/j.mechmat.2004.03.008.
- [23] R.A. Sauer and M. Holl. A detailed 3D finite element analysis of the peeling behaviour of a gecko spatula. *Comput. Methods Biomech. Biomed. Engin.*, 16(6):577–591, 2013. doi: 10.1080/10255842.2011.628944.
- [24] K. Autumn, A. Dittmore, D. Santos, and M. Spenko, M. Cutkosky. Frictional adhesion: a new angle on gecko attachment. *J. Exp. Biol.*, 209(18):3569–3579, 2006. doi: 10.1242/jeb.02486.

- [25] Q.H. Cheng, B. Chen, H.J. Gao, and Y.W. Zhang. Sliding-induced non-uniform pre-tension governs robust and reversible adhesion: a revisit of adhesion mechanisms of geckos. *J. R. Soc. Interface*, 9(67):283–291, 2012. doi: 10.1098/rsif.2011.0254.
- [26] Z. Peng and S. Chen. Effect of pre-tension on the peeling behavior of a bio-inspired nano-film and a hierarchical adhesive structure. *Appl. Phys. Lett.*, 101(16):163702, 2012. doi: 10.1063/1.4758481.
- [27] S. Hu, S. Lopez, P.H. Niewiarowski, and Z. Xia. Dynamic self-cleaning in gecko setae via digital hyperextension. *J. R. Soc. Interface*, 9(76):2781–2790, 2012. doi: 10.1098/rsif.2012.0108.
- [28] M.R. Begley, R.R. Collino, J.N. Israelachvili, and R.M. McMeeking. Peeling of a tape with large deformations and frictional sliding. *J. Mech. Phys. Solids*, 61(5):1265–1279, 2013. doi: 10.1016/j.jmps.2012.09.014.
- [29] R.R. Collino, N.R. Phillips, M.N. Rossol, R.M. McMeeking, and M.R. Begley. Detachment of compliant films adhered to stiff substrates via van der Waals interactions: role of frictional sliding during peeling. *J. R. Soc. Interface*, 11(97):20140453, 2014. doi: 10.1098/rsif.2014.0453.
- [30] S. Gouravaraju, R.A. Sauer, and S.S. Gautam. Investigating the normal and tangential peeling behaviour of gecko spatulae using a coupled adhesion-friction model. *J. Adhes.*, pages 1–32, 2020. doi: 10.1080/00218464.2020.1719838.
- [31] J.A. Williams and J.J. Kauzlarich. The influence of peel angle on the mechanics of peeling flexible adherends with arbitrary load–extension characteristics. *Tribol. Int.*, 38(11-12):951–958, 2005. doi: 10.1016/j.triboint.2005.07.024.
- [32] Z. Peng, H. Yin, Y. Yao, and S. Chen. Effect of thin-film length on the peeling behavior of film-substrate interfaces. *Phys. Rev. E*, 100(3):032804, 2019. doi: 10.1103/PhysRevE.100.032804.
- [33] A.M. Garner, A.Y. Stark, S.A. Thomas, and P.H. Niewiarowski. Geckos go the Distance: Water’s Effect on the Speed of Adhesive Locomotion in Geckos. *J. Herpetol.*, 51(2):240–244, 2017. doi: 10.1670/16-010.
- [34] R.A. Sauer. A Survey of Computational Models for Adhesion. *J. Adhes.*, 92(2):81–120, 2016. doi: 10.1080/00218464.2014.1003210.
- [35] G. Yagawa and H. Okuda. Neural networks in computational mechanics. *Arch. Comput. Methods Eng.*, 3(4):435–512, 1996. doi: 10.1007/BF02818935.
- [36] R. Hambli. Numerical procedure for multiscale bone adaptation prediction based on neural networks and finite element simulation. *Finite Elem. Anal. Des.*, 47(7):835–842, 2011. doi: 10.1016/j.finel.2011.02.014.
- [37] N. Sengupta, Md. Sahidullah, and G. Saha. Lung sound classification using cepstral-based statistical features. *Comput. Biol. Med.*, 75:118–129, 2016. doi: 10.1016/j.combiomed.2016.05.013.
- [38] E. Alizadeh, S.M. Lyons, J.M. Castle, and A. Prasad. Measuring systematic changes in invasive cancer cell shape using Zernike moments. *Integr. Biol.*, 8(11):1183–1193, 2016. doi: 10.1039/C6IB00100A.
- [39] A. Oishi and G. Yagawa. Computational mechanics enhanced by deep learning. *Comput. Methods Appl. Mech. Eng.*, 327:327–351, 2017. doi: 10.1016/j.cma.2017.08.040.
- [40] S. Islam and A. Kim. Machine Learning Enabled Wearable Brain Deformation Sensing System. In *2019 IEEE Signal Process. Med. Biol. Symp.*, pages 1–3. IEEE, 2019. doi: 10.1109/SPMB47826.2019.9037843.
- [41] B. Sattari Baboukani, Z. Ye, K. G. Reyes, and P. C. Nalam. Prediction of nanoscale friction for two-dimensional materials using a machine learning approach. *Tribol. Lett.*, 68:57, 2020. doi: <https://doi.org/10.1007/s11249-020-01294-w>.
- [42] I.E. Lagaris, Aristidis Likas, and D.I. Fotiadis. Artificial neural networks for solving ordinary and partial differential equations. *IEEE Trans. Neural Networks*, 9(5):987–1000, 1998. doi: 10.1109/72.712178.
- [43] S.J.S. Hakim and H. Abdul Razak. Structural damage detection of steel bridge girder using artificial neural networks and finite element models. *Steel Compos. Struct.*, 14(4):367–377, 2013. doi: 10.12989/scs.2013.14.4.367.
- [44] H. Sadegh, A.N. Mehdi, and A. Mehdi. Classification of acoustic emission signals generated from journal bearing at different lubrication conditions based on wavelet analysis in combination with artificial neural network and genetic algorithm. *Tribol. Int.*, 95:426–434, 2016. doi: 10.1016/j.triboint.2015.11.045.
- [45] L. Liang, M. Liu, C. Martin, and W. Sun. A deep learning approach to estimate stress distribution: a fast and accurate surrogate of finite-element analysis. *J. R. Soc. Interface*, 15(138):20170844, 2018. doi: 10.1098/rsif.2017.0844.
- [46] J. Zurada. *Introduction to Artificial Neural Systems*. West Publishing Co., USA, 1992.
- [47] S. Yoshimura, A. Matsuda, and G. Yagawa. New regularization by transformation for neural network based inverse analyses and its application to structure identification. *Int. J. Numer. Methods Eng.*, 39(23):3953–3968, 1996. doi: 10.1002/(SICI)1097-0207(19961215)39:23<3953::AID-NME31>3.0.CO;2-O.
- [48] R. Lopez, E. Balsa-Canto, and E. Oñate. Neural networks for variational problems in engineering. *Int. J. Numer. Methods Eng.*, 75(11):1341–1360, 2008. doi: 10.1002/nme.2304.
- [49] T. Furukawa and G. Yagawa. Implicit constitutive modelling for viscoplasticity using neural networks. *Int. J. Numer. Methods Eng.*, 43(2):195–219, 1998. doi: 10.1002/(SICI)1097-0207(19980930)43:2<195::AID-NME418>3.0.CO;2-6.
- [50] N. Huber and Ch. Tsakmakis. A neural network tool for identifying the material parameters of a finite deformation viscoplasticity model with static recovery. *Comput. Methods Appl. Mech. Eng.*, 191(3-5):353–384, 2001. doi: 10.1016/S0045-7825(01)00278-X.
- [51] H. Man and T. Furukawa. Neural network constitutive modelling for non-linear characterization of anisotropic materials. *Int. J. Numer. Methods Eng.*, 85(8):939–957, 2011. doi: 10.1002/nme.2999.
- [52] Xueyang Li, Christian C. Roth, and Dirk Mohr. Machine-learning based temperature- and rate-dependent plasticity model: Application to analysis of fracture experiments on dp steel. *Int. J. Plast.*, 118:320–344, 2019. doi: <https://doi.org/10.1016/j.ijplas.2019.02.012>. URL <http://www.sciencedirect.com/science/article/pii/S0749641918306983>.
- [53] S.W. Liu, Jin H. Huang, J.C. Sung, and C.C. Lee. Detection of cracks using neural networks and computational mechanics. *Comput. Methods Appl. Mech. Eng.*, 191(25-26):2831–2845, 2002. doi: 10.1016/S0045-7825(02)00221-9.
- [54] J. Zacharias, C. Hartmann, and A. Delgado. Damage detection on crates of beverages by artificial neural networks trained with finite-element data. *Comput. Methods Appl. Mech. Eng.*, 193(6-8):561–574, 2004. doi: 10.1016/j.cma.2003.10.009.
- [55] L. Manevitz, M. Yousef, and D. Givoli. Finite-Element Mesh Generation Using Self-Organizing Neural Networks. *Comput. Civ. Infrastruct. Eng.*, 12(4):233–250, 1997. doi: 10.1111/0885-9507.00060.

- [56] M. P. Rapetto, A. Almqvist, R. Larsson, and P. M. Lugt. On the influence of surface roughness on real area of contact in normal, dry, friction free, rough contact by using a neural network. *Wear*, 266(5):592–595, 2009. doi: <https://doi.org/10.1016/j.wear.2008.04.059>. URL <http://www.sciencedirect.com/science/article/pii/S0043164808003177>.
- [57] L.A. Gyurova and K. Friedrich. Artificial neural networks for predicting sliding friction and wear properties of polyphenylene sulfide composites. *Tribol. Int.*, 44(5):603–609, 2011. doi: 10.1016/j.triboint.2010.12.011.
- [58] K.M. Hamdia, H. Ghasemi, Y. Bazi, H. AlHichri, N. Alajlan, and T. Rabczuk. A novel deep learning based method for the computational material design of flexoelectric nanostructures with topology optimization. *Finite Elem. Anal. Des.*, 2019. doi: 10.1016/j.finela.2019.07.001.
- [59] Grace X. Gu, Chun-Teh Chen, Deon J. Richmond, and Markus J. Buehler. Bioinspired hierarchical composite design using machine learning: simulation, additive manufacturing, and experiment. *Mater. Horiz.*, 5:939–945, 2018. doi: 10.1039/C8MH00653A. URL <http://dx.doi.org/10.1039/C8MH00653A>.
- [60] A. Oishi and S. Yoshimura. A new local contact search method using a multi-layer neural network. *Comput. Model. Eng. Sci.*, 2007. doi: 10.3970/cmesci.2007.021.093.
- [61] A. Oishi and G. Yagawa. A surface-to-surface contact search method enhanced by deep learning. *Comput. Mech.*, 65(4):1125–1147, 2020. doi: 10.1007/s00466-019-01811-2.
- [62] D. Nowell and P.W. Nowell. A machine learning approach to the prediction of fretting fatigue life. *Tribol. Int.*, 141:105913, 2020. doi: 10.1016/j.triboint.2019.105913.
- [63] Yongtae Kim, Charles Yang, Youngsoo Kim, Grace X. Gu, and Seunghwa Ryu. Designing an adhesive pillar shape with deep learning-based optimization. *ACS Appl. Mater. Interf.*, 12(21):24458–24465, 2020. doi: 10.1021/acsami.0c04123. URL <https://doi.org/10.1021/acsami.0c04123>.
- [64] A. R. Khoei, H. Moslemi, and M. R. Seddighian. An efficient stress recovery technique in adaptive finite element method using artificial neural network. *Eng. Fract. Mech.*, 237:107231, 2020. ISSN 0013-7944. doi: <https://doi.org/10.1016/j.engfracmech.2020.107231>. URL <http://www.sciencedirect.com/science/article/pii/S0013794420308146>.
- [65] J. A. Nelder and R. Mead. A simplex method for function minimization. *The Computer Journal*, 7(4):308–313, 1965. doi: 10.1093/comjnl/7.4.308. URL <https://doi.org/10.1093/comjnl/7.4.308>.
- [66] I.I. Argatov and Y.S. Chai. An artificial neural network supported regression model for wear rate. *Tribol. Int.*, 138:211–214, 2019. doi: 10.1016/j.triboint.2019.05.040.
- [67] D.J.C. MacKay. A Practical Bayesian Framework for Backpropagation Networks. *Neural Comput.*, 4(3):448–472, 1992. doi: 10.1162/neco.1992.4.3.448.
- [68] F. Burden and D. Winkler. Bayesian Regularization of Neural Networks. In *Methods Mol. Biol.*, pages 23–42. Humana Press, 2008. doi: 10.1007/978-1-60327-101-1\_3.
- [69] L.M. Saini and M.K. Soni. Artificial neural network based peak load forecasting using Levenberg–Marquardt and quasi-Newton methods. *IEEE Proc. - Gener. Transm. Distrib.*, 149(5):578, 2002. doi: 10.1049/ip-gtd:20020462.
- [70] M. Kayri. Predictive Abilities of Bayesian Regularization and Levenberg–Marquardt Algorithms in Artificial Neural Networks: A Comparative Empirical Study on Social Data. *Math. Comput. Appl.*, 21(2):20, 2016. doi: 10.3390/mca21020020.
- [71] M. Lefik and B.A. Schrefler. Artificial neural network as an incremental non-linear constitutive model for a finite element code. *Comput. Methods Appl. Mech. Eng.*, 192(28-30):3265–3283, 2003. doi: 10.1016/S0045-7825(03)00350-5.
- [72] H.-F Li and S.-Y. Lee. Mining frequent itemsets over data streams using efficient window sliding techniques. *Expert Syst. Appl.*, 36(2):1466–1477, 2009. doi: 10.1016/j.eswa.2007.11.061.
- [73] J.L. Ticknor. A Bayesian regularized artificial neural network for stock market forecasting. *Expert Syst. Appl.*, 40(14):5501–5506, 2013. doi: 10.1016/j.eswa.2013.04.013.
- [74] S. Koroglu, P. Sergeant, and N. Umurkan. Comparison of analytical, finite element and neural network methods to study magnetic shielding. *Simul. Model. Pract. Theory*, 18(2):206–216, 2010. doi: 10.1016/j.simpat.2009.10.007.
- [75] K. Yang and M. Xiong. Prediction of CH<sub>4</sub> adsorption on different activated carbons by developing an optimal multilayer perceptron artificial neural network. *Energy Sources, Part A Recover. Util. Environ. Eff.*, 41(17):2061–2072, 2019. doi: 10.1080/15567036.2018.1549161.
- [76] R. A. Sauer and J. C. Mergel. A geometrically exact finite beam element formulation for thin film adhesion and debonding. *Finite Elem. Anal. Des.*, 86:120–135, 2014. doi: 10.1016/j.finela.2014.03.009.
- [77] S. Gouravaraju, R.A. Sauer, and S.S. Gautam. On the presence of a critical detachment angle in gecko spatula peeling - a numerical investigation using an adhesive friction model. *J. Adhes.*, 2020. doi: <http://dx.doi.org/10.1080/00218464.2020.1746652>.
- [78] R.A. Sauer and S. Li. A contact mechanics model for quasi-continua. *Int. J. Numer. Methods Eng.*, 71(8):931–962, 2007. doi: 10.1002/nme.1970.
- [79] J.C. Mergel, R. Sahli, J. Scheibert, and R.A. Sauer. Contact with coupled adhesion and friction: computational framework, applications, and new insights. *J. Mech. Phys. Solids*, 146:104194, 2021. doi: 10.1016/j.jmps.2020.104194.
- [80] R.A. Sauer and P. Wriggers. Formulation and analysis of a three-dimensional finite element implementation for adhesive contact at the nanoscale. *Comput. Methods Appl. Mech. Eng.*, 198(49-52):3871–3883, 2009. doi: 10.1016/j.cma.2009.08.019.
- [81] J. Bonet and R.D. Wood. *Nonlinear Continuum Mechanics for Finite Element Analysis*. Cambridge University Press, London, 2nd edition, 2008.
- [82] R.A. Sauer. Enriched contact finite elements for stable peeling computations. *Int. J. Numer. Methods Eng.*, 87(6):593–616, 2011. doi: 10.1002/nme.3126.
- [83] H.B. Demuth, M.H. Beale, O. De Jess, and M.T. Hagan. *Neural network design*. Martin Hagan, 2nd edition, 2014.
- [84] A.N. Tikhonov. Solution of ill-posed problems and the regularization method. *Dokl. Akad. Nauk SSSR*, 151:501–504, 1963.
- [85] F. Dan Foresee and M.T. Hagan. Gauss-Newton approximation to Bayesian learning. In *Proc. Int. Conf. Neural Networks*, volume 3, pages 1930–1935. IEEE, 1997. doi: 10.1109/ICNN.1997.614194.